Fracture resistance enhancement of layered structures by multiple cracks

Goutianos, Stergios; Sørensen, Bent F.

Published in:
Engineering Fracture Mechanics

Link to article, DOI:
10.1016/j.engfracmech.2015.10.036

Publication date:
2016

Document Version
Peer reviewed version

Fracture Resistance Enhancement of Layered Structures by Multiple Cracks

Stergios Goutianos, Bent F. Sørensen*

Department of Wind Energy, Section of Composites and Materials Mechanics, Technical University of Denmark, Risø Campus, DK-4000 Roskilde, Denmark

Abstract

A theoretical model is developed to test if the fracture resistance of a layered structure can be increased by introducing weak layers changing the cracking mechanism. An analytical model, based on the J integral, predicts a linear dependency between the number of cracks and the steady state fracture resistance. A finite element cohesive zone model, containing two cracking planes for simplicity, is used to check the theoretical model and its predictions. It is shown that for a wide range of cohesive law parameters, the numerical predictions agree well quantitatively with the theoretical model. Thus, it is possible to enhance considerably the fracture resistance of a structure by adding weak layers.

Keywords: Multiple Cracks; Fracture Resistance; Delamination; J Integral; Cohesive Law;

1. Introduction

Layered structures/materials often exhibit low interlaminar fracture resistance and are therefore susceptible to delamination when loaded. Through-thickness stresses, arising for example from manufacturing defects or geometric discontinuities, can result in propagation of interlaminar cracks which may lead to a substantial decrease in the structural integrity of a component [1, 2].

*Corresponding author

Email addresses: goutianos@gmail.com (Stergios Goutianos), bsqr@dtu.dk (Bent F. Sørensen)

As a result, many techniques have been developed to improve the through-thickness fracture resistance of layered structures and materials *e.g.* fibre reinforced polymer composites. However, at the same time, the in-plane properties are usually adversely affected [3]. In the field of composite materials, the research in developing damage tolerant composites can be categorized into two directions: a) material improvements and b) modifications of the fibre architecture.

Material improvements include modified/tougher matrices [4–7], effect of fibre/matrix interface [8–11] and interleaving concepts [12–16]. The alternative approach of modification of the fibre architecture includes stitching [17], knitting [18, 19], weaving and braiding [20, 21] of textiles laminates or z-pinning [3] usually for prepreg laminates [22, 23].

All the above techniques aim, in general, to increase the fracture resistance of damage prone areas by making the damage prone areas stronger or tougher. In the present paper, an alternative approach is proposed, motivated by recent experimental work of Rask and Sørensen [24]. Testing Double Cantilever Beam (DCB) specimens, they observed that by changing the ply thicknesses of glass fibre/polyester composite beams bonded together with a thermoset adhesive, more delamination cracks could develop next to the adhesive/laminate crack. The overall steady-state fracture resistance was found to increase proportionally to the number of secondary cracks. These results suggest that a linear relationship may exist between the number of crack tips/fracture process zones and the overall steady state fracture resistance values.

Thus, in the present work, we explore the possibility of increasing the overall fracture resistance of a layered structure by introducing weak planes that result in multiple delaminations next to the damage prone areas as shown in Fig. 1. In many cases such as in fibre composite materials [11] or in adhesive joints between composite laminates [25], crack growth/delamination involves large scale fibre bridging, which is a large-scale fracture process zone and thus it should not be characterised by linear elastic fracture mechanics. The problem is analysed by an analytical model and by a numerical model (cohesive zone modelling implemented in a finite element framework) using a DCB specimen subjected to pure bending moments shown in Fig. 2. Both the analytical and numerical model are valid for large-scale fracture process zones. In Fig. 2, the secondary crack represents the potential crack path of the weak plane introduced in the vicinity of the primary crack which may represent for example an adhesive layer/joint. The cohesive zone parameters

of the secondary crack that lead to overall fracture resistance enhancement are determined. In order to keep the parameter study simple, the focus is on only two delamination planes, a primary and a secondary crack plane as shown in Fig. 1. In addition, it will be demonstrated that it is possible to quantify the maximum possible increase in overall fracture resistance through an analytical fracture mechanics model including n delaminations based on the J integral [26]. Toughness increase induced by a crack jumping was also recently reported by [27] using cohesive zone modelling, whereas toughening due to microcracks (microcrack shielding) under linear elastic fracture mechanics conditions was extensively studied for brittle materials [28, 29].

2. Analysis

The mechanism of formation of multiple delaminations is analysed in this Section using the specimen of Fig. 2.

2.1. Concept of cohesive laws

The fracture process zone of the primary and secondary cracks can be modelled by a cohesive zone model [30–32]. The tractions transferred across the crack faces of the fracture process zone can be described by cohesive laws or traction-separation laws shown in Fig. 3 for pure Mode I and Mode II ($i = 1$ for the primary crack and $i = 2$ for the secondary crack).

The local normal tractions σ_n^i and the local shear tractions σ_t^i in the fracture process zone are functions of the local crack openings in the normal and tangential directions, denoted by δ_n^i and δ_t^i, respectively. The peak tractions before damage develops and crack opening begins are denoted by $\hat{\sigma}_n^i$ and $\hat{\sigma}_t^i$. The cohesive tractions reduce to zero when the openings reach the critical values, $\delta_n^{c,i}$ and $\delta_t^{c,i}$, respectively.

2.2. Problem Statement

Fig. 4 shows the area ahead of the notch (at distance ℓ) of the specimen of Fig. 2. Under monotonically increasing applied load (moment), the normal traction (along $x_2 = 0$) increases continuously. The shear tractions parallel to the crack are ignored in this Section, as the problem of Fig. 2 is Mode I dominated. As the normal stress at the tip of the notch reaches the normal peak traction, $\hat{\sigma}_n^1$, as shown in Fig. 4a, the primary crack is begins to open *i.e.* the fracture process zone forms. At distance h, where the potential secondary crack lies, the normal stress, σ_{22}, at any material point along this plane, is

initially assumed to be lower than the peak traction for the secondary crack, $\sigma_{22} < \hat{\sigma}_n^2$ and thus there is no crack formation.

The fracture process zone of the primary crack evolves (see Fig. 4b) with increasing applied load, increasing the tractions next to the primary crack plane. The normal opening at the end of the fracture process zone is denoted by $\delta_n^{*,1}$. If the normal stress at any point within the cohesive zone of the secondary plane reaches the peak traction of the secondary crack, $\sigma_{22} = \hat{\sigma}_n^2$, the secondary crack forms close to the current tip of the primary crack. Upon further increase of the applied moment, both the primary and secondary cracks grow, possibly at different rates, and eventually are fully developed, $\delta_n^{*,1} \geq \delta_n^{c,1}$ and $\delta_n^{*,2} \geq \delta_n^{c,2}$, and steady-state is reached as shown in Fig. 5. A complication is that both the left hand and the right hand crack tips can propagate. The left hand crack tip propagates in the negative x_1 - direction and the right hand crack tip propagates in the positive x_1 - direction. The combined work per unit area of the tractions behind the crack tip is denoted by J_{ss}^i with $i = 1$ for the primary crack and $i = 2$ for the secondary crack.

2.3. J integral analysis

We now wish to investigate the effect of the secondary crack on the overall fracture resistance, J_R. To derive the overall fracture resistance of the problem depicted in Fig. 4, the path independent J integral [26] is used. The J integral is defined as [26]:

$$J = \int_\Gamma \Phi dx_2 + \sigma_{ij} n_j \frac{\partial u_i}{\partial x_1} dS \tag{1}$$

where Φ is the strain energy density, σ_{ij} the stress tensor, u_i the displacement vector, n_j the normal unit vector to the integration path Γ. The J integral is path-independent, *i.e.* J takes the same value when evaluated along a path along the external boundaries Γ_{ext} and along a local path just outside the fracture process zone Γ_{loc}. Fig. 6 shows the local path Γ_{loc} around the fracture process zone than encloses both the primary and secondary crack.

First, we analyze the situation of a primary crack with no secondary crack yet developed, as shown schematically in Fig. 6(a). The path-independent J integral [26] is evaluated along an integration path, Γ_{loc}^1, that runs locally along the primary crack in a counter-clock-wise direction. The results is [26]:

$$J^1_{loc} = \int_0^{\delta^{*1}_n} \sigma^1_n(\delta^1_n) d\delta^1_n, \tag{2}$$

where δ^{*1}_n is the end-opening of the cohesive zone. For the fully-developed cohesive zone, $\delta^{*1}_n = \delta^{c,1}_n$ so that:

$$J^1_{loc} = \int_0^{\delta^{c,1}_n} \sigma^1_n(\delta^1_n) d\delta^1_n = J^1_{n,ss}. \tag{3}$$

In Eq. 3, the integral, the area under the traction-separation curves, is the work of the cohesive traction and $J^1_{n,ss}$ is the steady-state fracture resistance of the primary crack.

Next, we analyze the situation of having both a primary crack and a secondary crack extending from $x_1 = x^-_1$ to $x_1 = x^+_1$, as shown in Fig. 6(b). We wish to use an integration path just outside the cracks and fracture process zones, so that by path-independence we can set $J_{loc} = J_{ext}$. The chosen integration path consists of parts of Γ^1_{loc} from x_1 to x^h_1, where it cuts across the ligament using the path Γ^-_h (in the negative x_2-direction), to path Γ^{2-}_{loc}, at the secondary crack. The path Γ^{2-}_{loc} starts from $(x_1; x_2) = (x^h_1; -h)$ and runs in the negative x_1-direction to $x_1 = x^-_1$, loops around the left hand side crack tip and continues in the positive x_1-direction to $x_1 = x^h_1$. Another integration path denoted Γ^{2+}_{loc} continues from x^h_1 to the right hand side crack tip at $x_1 = x^+_1$ where it loops around the crack tip and continues in the negative x_1-direction to $x_1 = x^h_1$. The integration path continues in the positive x_2-direction along Γ^+_h up to the integration path of the primary crack, Γ^1_{loc}, and continues in the anti-clock direction along the rest of the path Γ^1_{loc}. Then, a J integral evaluation along the entire path can be written as:

$$J_{loc} = J^1_{loc} + J^-_h + J^{2-}_{loc} + J^{2+}_{loc} + J^+_h \tag{4}$$

For a fully-developed primary crack the J integral equation for Γ^1_{loc} is identical to Eq. 3.

The integration paths Γ^-_h and Γ^+_h are identical except for the integration path direction. Therefore, $J^-_h = -J^+_h$ and therefore J^-_h and J^+_h cancel out in Eq. 4.

For J^{2+}_{loc}, the integration path runs locally along the crack faces of right hand side of the secondary crack in a counter-clock-wise direction, which is

the conventional J-integral problem. The results for the fully-developed cohesive zone situation, where $\delta_n^{*,1} = \delta_n^{c,1}$ and $\delta_n^{*,2} = \delta_n^{c,2}$, is - analogous to Eq. 3:

$$J_{loc}^{2+} = \int_0^{\delta_n^{c,2}} \sigma_n^2(\delta_n^2) d\delta_n^2 = J_{n,ss}^2. \tag{5}$$

In contrast, J_{loc}^{2-} is a J-integral evaluation of a left hand side crack (*i.e.*, pointing towards the negative x_1 direction). Therefore we show more details in this derivation. The integral consists of two parts, one from the upper crack face and one for the lower crack face.

Since $dS = -dx_1$ and $n_j^+ = (0; 1; 0)$ for the upper crack face and $dS = dx_1$ and $n_j^- = (0; -1; 0)$ for the lower crack face we get:

$$J_{loc}^{2-} = \int_{x_1^h}^{x_1^-} -\sigma_{22} n_2^+ \frac{\partial u_2^+}{\partial x_1}(-dx_1) + \int_{x_1^-}^{x_1^h} -\sigma_{22} n_2^- \frac{\partial u_2^-}{\partial x_1}(dx_1) \tag{6}$$

With $n_2^+ = 1$ and $n_2^- = -1$ and defining the opening displacement as $\delta_n^2 = u_2^+ - u_2^-$, where u_2^+ is the displacement in the x_2-direction of the upper crack face of the secondary crack and u_2^- is the displacement in the x_2-direction of the lower crack face of the secondary crack we obtain:

$$J_{loc}^{2-} = \int_{x_1^h}^{x_1^-} \sigma_{22} \left(\frac{\partial u_2^+}{\partial x_1} - \frac{\partial u_2^-}{\partial x_1} \right) dx_1 = \int_{x_1^h}^{x_1^-} \sigma_{22} \frac{\partial \delta_n^2}{\partial x_1} dx_1 \tag{7}$$

Furthermore, by the Chain rule:

$$d\delta_n^2 = \frac{\partial \delta_n^2}{\partial x_1} dx_1, \tag{8}$$

we change integration variables and integration limits, noting that $\sigma_{22} = \sigma_n^2$ and, for the fully developed cohesive law, the end-opening is equal to the critical separation, $\delta_n^{*2-} = \delta_n^{c,2}$. Then we get:

$$J_{loc}^{2-} = \int_{\delta_n^{*2-}}^{0} \sigma_n^2(\delta_n^2) d\delta_n^2 = -\int_0^{\delta_n^{c,2}} \sigma_n^2(\delta_n^2) d\delta_n^2 \tag{9}$$

Comparing the J integral terms, we note that J_{loc}^{2-} from Eq. 9 and J_{loc}^{2+} from Eq. 5 cancel out when inserting into Eq. 4. Then:

$$J_{loc} = J_{loc}^1. \tag{10}$$

Thus, in case the secondary crack propagates in both ends, the work of separation along path Γ_{loc}^{2-} of the secondary crack contributes negative to the J integral and outbalances the toughness enhancement from path Γ_{loc}^{2+}. The overall fracture resistance J_R is then equal to the fracture resistance of the primary crack even though the secondary crack propagates (in both directions). [1]

In the above J integral analysis, it is assumed that the secondary crack extends in both directions. An alternative situation is when the secondary crack extends only to the right hand side. The left hand side does not grow *i.e.* the crack does not open and the crack tip remains at its initial position. In this case the J integral contribution from the bridging tractions at the left hand side crack tip is zero ($J_{n,ss}^{2} = 0$). Then, Eq. 9 becomes:

$$J_{loc}^{2-} = 0 \tag{11}$$

and Eq. 4 gives:

$$J_{loc} = J_{loc}^{1} + J_{loc}^{2+} = J_{n,ss}^{1} + J_{n,ss}^{2} \tag{12}$$

Thus, in this case the overall steady-state fracture resistance, $J_{R,ss}$, is increased by $J_{n,ss}^{2}$. Thus, if the left hand side crack tip of the secondary crack remains closed, its right hand side crack tip provides a direct contribution to the overall steady-state fracture resistance.

Eq. 12 can be generalised to N secondary (delamination) cracks:

$$J_{loc} = J_{n,ss}^{1} + N J_{n,ss}^{2} \tag{13}$$

Eq. 13 demonstrates that there is significant potential enhancement of the overall fracture resistance by having multiple weak planes next to a damage prone area. The overall steady-state fracture resistance, $J_{R,ss}$, will increase linearly with the number of secondary cracks which is in agreement with the experimental observations [24].

[1] Eq. 9 should not be understood as the work (per unit area) of the cohesive traction as the crack advances in the x_1 direction (implying crack tip translation in that direction, *i.e.* crack closure at the left hand side crack tip). For a left hand side crack tip advancing in the negative x_1 direction the J integral contribution J_{loc}^{2-} should in fact be negative as can be assessed by analysing any left hand side crack tip by the J integral.

The assumption that the left hand side of the secondary crack does not open can be relaxed and allow an initial opening, followed by unloading. During unloading, as the left hand side of the secondary crack unloads, the bridging tractions decrease, approaching zero for complete crack closure. Then, Eq. 12 still holds true.

It is interesting to note that such a linear relationship (as upper bound) was also predicted for one and two secondary cracks under linear elastic fracture mechanics [29].

The J integral analysis presented in this Section sets an upper limit of the overall fracture resistance enhancement, Eq. 12, and a lower limit, Eq. 10, depending on the behaviour of the left hand side of the secondary crack. In the next Section, cohesive zone modelling is used to determine which case is more realistic for the secondary crack *i.e.* fully developed or closed left hand side crack tip. The real situation is likely to be somewhere between the two bounds, depending on the openings details of the left hand crack tip of the secondary crack. In the next Section, the cohesive zone modelling details are presented.

3. Numerical model

3.1. Geometry and loading

The crack growth problem of Fig. 2 was modelled by the finite element method using the commercial code Abaqus, version 6.11 [33] as a plane strain problem (see Fig. 7).

The right hand side of the specimen is fully constrained ($u_1 = u_2 = 0$ at $x_1 = L - \ell$). As long as the crack tip is far away from the right hand side specimen end, the boundary conditions at the right hand side should not affect the crack growth in the specimen. Pure bending moments (external loading) are applied to left hand side beams by prescribing the rotational displacements of two points, which are tied to two analytical rigid surfaces tied to the beams [34]. The two beams are modelled as plane strain isotropic linear-elastic solids. Four-node elements and triangular three-node reduced integrations elements are used in order to control the mesh transition and to keep the element number of low.

Convergence difficulties are commonly observed when modelling crack growth with implicit finite element methods. A number of numerical stability methods exist to overcome these difficulties, however an explicit FE method is more robust [35]. In the present study, an explicit solver was used to solve

the problem under quasi-static conditions using mass-scaling [25]. In the solution procedure, viscous damping was also necessary for convergence. In all simulations, it was ensured that the sum of the kinetic energy and the energy dissipated by viscosity was less than 0.5% of the strain energy.

For the specimen of Fig. 7, following the analysis of [36] for pure Mode I loading, the J integral evaluated along the external boundaries, under plane strain conditions and mixed-mode loading, is [37]:

$$J_{ext} = (1-\nu^2)\frac{21(M_1^2+M_2^2)-6M_1M_2}{4B^2H^3E} \tag{14}$$

where H and B are the height and width of the specimen respectively, E and ν are the Youngs' modulus and Poisson's ratio of the beams and the moments M_1 and M_2 applied to the left hand cracked ends are taken positive in the same direction. This result is valid only as long as the secondary crack remains away from the left hand end of the beam so that the beams ends are subjected to pure bending. The specimen of Fig. 7 is not symmetric when the secondary crack has developed/formed. Thus, magnitude of the reaction moment, M_1, in the upper beam is different from that of the reaction moment, M_2, in the lower beam of the specimen although the prescribed rotational displacements are equal and of opposite sign. Since, M_1 is not quite equal to $-M_2$ (the difference between $|M_1|$ and $|M_2|$ is typically less than 5%), there is a tangential crack opening. However, it will be shown later that this opening is negligible in comparison with the normal opening of the primary and secondary cracks. As can be seen from Eq. 14 the J integral equation is independent of the crack length. Thus, by extracting the moments from the finite element solution, the overall fracture resistance, J_R, given by the J integral can be directly evaluated.

3.2. Cohesive Zone Modelling

In the finite element model, the entire potential planes for the primary and secondary cracks are modelled with cohesive elements of finite thickness corresponding to 0.1% of H to avoid interpenetration of the two surfaces adjacent to the cohesive elements [25]. As can be seen from Fig. 7, the cohesive zone of the potential secondary crack plane extends along the whole length the specimen, L, allowing crack growth behind the initial notch (primary crack).

The cohesive laws are taken to have a bilinear shape. Fig. 8 shows the pure normal and shear cohesive laws for each crack where σ_n and σ_t

are the normal and shear tractions, δ_n and δ_t the normal and tangential openings. The cohesive laws have initial rising parts with stiffness K_n^i and K_t^i for the primary and secondary cracks which are assigned high values ($K_n^i H/E = K_t^i H/E = 2.5\times10^{-3}$) to practically have linear softening cohesive laws with minimum opening prior to crack opening (see Fig. 3). In all simulations the normal and shear peak tractions of the primary crack are constant and equal to $\hat{\sigma}_n^1/E = \hat{\sigma}_t^1/E = 5 \times 10^{-5}$.

In the analytical model of the previous Section only the normal opening of the cracks is considered. In the finite element model, however, both the normal and tangential openings of the cracks are taken into account (see Fig. 8). Following the mixed-mode model of [38] and [39], it is assumed that normal and shear cohesive laws are totally uncoupled, except being coupled through a simple failure criterion of the form [40]:

$$F_{cr} = \frac{W_n^i}{J_{n,ss}^i} + \frac{W_t^i}{J_{t,ss}^i} = 1, \quad i = 1 \quad or \quad 2 \tag{15}$$

where $J_{n,ss}^i$ and $J_{t,ss}^i$ are the Mode I and Mode II steady-state fracture resistances for the primary ($i = 1$) and for the secondary crack ($i = 2$) and represent the total area under the cohesive laws for each mode (Fig. 8). The work of the cohesive tractions (shaded area in Fig. 8) are denoted W_n and W_t for the normal and shear tractions, respectively. With the uncoupled cohesive laws chosen, W_n and W_t depend only on δ_n^* and δ_t^*, respectively.

The uncoupled, path-independent mixed-mode model of Eq. 15 is preferred since the Abaqus [33] implemented mixed-mode model is a truss-like cohesive law (the traction vector is specified to follow the direction of the crack opening displacement vector) which is path dependent, *i.e.* the combined work of the cohesive tractions depends on the opening path history except for the cases that the mixed mode cohesive law is the same in all directions [41]. Thus, a user defined material subroutine was implemented for the model of Eq. 15 used with the Abaqus cohesive elements. Since one basic assumption of the analytical model is that the left hand side of the secondary crack can unload, it is important that unloading is implemented in the subroutine. In the present study, we use a linear unloading to zero, as shown with dotted lines in Fig. 8.

4. Numerical results

4.1. Effect of the peak traction of the secondary crack

Fig. 9 shows some typical overall fracture resistance curves, J_R, as a function of the end-opening Δ_n for h/H equal to 0.01 and 0.1, predicted by the finite element method. J_R is calculated from Eq. 14 using the moments M_1 and M_2 extracted from the FE model. Δ_n is the displacement difference between the upper crack face of the primary crack and the lower surface of the secondary crack at the end of the notch (points a and b in Fig. 7). Δ_n is thus approximately equal to the end-opening recorded in experiments [24, 25]. For both curves, the ratio $\hat{\sigma}_n^2/\hat{\sigma}_n^1$ is equal to 0.5. For both simulations, J_R increases to a steady-state value, denoted $J_{R,ss}$. For both curves, $J_{R,ss}$ exceeds the fracture energy of the primary crack $J_{n,ss}^1$. The steady-state value for $h/H = 0.01$ is higher than for $h/H = 0.1$ The numbers in circles are referred to in subsequent figures.

In Fig. 10 the primary and secondary crack openings are shown for four different loading history points (see Fig. 9). It can be seen that the right side secondary crack front lies ahead the crack front of the primary crack although the primary crack is the crack that opens first. Both the primary crack and the right hand side crack tip of the secondary crack open continuously. The left hand side of the secondary crack opens initially but as the crack grows to the right it closes/unloads again. This will be elaborated further in the next Section.

The computational results of Fig. 10 capture the salient features of experimental observations of [24].

Fig. 11 shows the overall steady-state fracture resistance, $J_{R,ss}$, for different peak tractions of the secondary crack at various distances h between the planes of the primary and secondary crack paths. For both cracks, the cohesive law for the normal traction is identical to the cohesive law for the shear traction ($\hat{\sigma}_n^i = \hat{\sigma}_t^i$ and $\delta_n^{c,i} = \delta_t^{c,i}$). The cohesive stiffnesses of the primary and secondary cracks are equal *i.e.* $K_n^1 = K_n^2$ and $K_t^1 = K_t^2$ and the steady-state fracture resistances are equal *i.e.* $J_{n,ss}^1 = J_{n,ss}^2$ and $J_{t,ss}^1 = J_{t,ss}^2$. Since the peak tractions of the secondary crack, $\hat{\sigma}_n^2$ and $\hat{\sigma}_t^2$, vary and $J_{n,ss}^1$ and $J_{n,ss}^2$ are held fixed, both characteristic cohesive law openings (Fig. 8) are different between the primary and secondary crack *i.e.* $\delta_n^{o,1} \neq \delta_n^{o,2}$, $\delta_t^{o,1} \neq \delta_t^{o,2}$, $\delta_n^{c,1} \neq \delta_n^{c,2}$ and $\delta_t^{c,1} \neq \delta_t^{c,2}$.

The computed overall steady-state fracture resistance values, $J_{R,ss}$, are within the theoretical lower and upper limits derived in previous Section (see

Eqs. 10 and 12).

From Fig. 11 we note that as expected, when the peak traction of the secondary crack is larger than the peak traction of the primary crack the secondary crack does not form. Only the primary crack opens and grows and as consequence the overall steady-state fracture resistance, $J_{R,ss}$, is equal to the steady-state fracture resistance of the primary crack, $J^1_{n,ss}$, for any distance h.

When the peak traction of the secondary crack is smaller that the peak traction of the primary crack ($\hat{\sigma}^2_n/\hat{\sigma}^1_n < 1$), then both the primary and the secondary crack open and grow simultaneously. With increasing h, the overall steady-state fracture resistance decreases for all $\hat{\sigma}^2_n/\hat{\sigma}^1_n$ ratios. In all cases, the overall steady-state fracture resistance, $J_{R,ss}$, is larger than the steady-state fracture resistance of the primary crack, $J^1_{n,ss}$. More interestingly, $J_{R,ss}$ approaches the upper bound (Eq. 12) for a large range of $\hat{\sigma}^2_n/\hat{\sigma}^1_n$ ratios and small h. When the peak traction of the secondary crack is much smaller than the peak traction of the primary crack ($\hat{\sigma}^2_n/\hat{\sigma}^1_n < 0.3$), the overall steady-state fracture resistance approaches approximately the same value for all distances h and it is closer to the lower limit (Eq. 10). Of the two non-dimensional parameters, $\hat{\sigma}^2_n/\hat{\sigma}^1_n$ and h/H, the later is the most important in the sense that for h/H sufficiently small, $J_{R,ss}$ is close to the upper bound for a wide range of $\hat{\sigma}^2_n/\hat{\sigma}^1_n$ values.

4.2. Effect of the steady-state fracture resistance of the secondary crack

In this Section we present results from simulations for which the steady-state fracture resistance of the secondary crack differs from the steady-state fracture resistance of the primary crack. As in the previous Section the Mode II cohesive law is identical to the Mode I cohesive law for each crack. Fig. 12 shows the overall steady-state fracture resistance, $J_{R,ss}$, as a function of the ratio of Mode I steady-state fracture resistance of the secondary crack, $J^2_{n,ss}$, over the Mode I steady-state fracture resistance of the primary crack, $J^1_{n,ss}$, for $h/H = 0.01$ and two $\hat{\sigma}^2_n/\hat{\sigma}^1_n$ ratios. It can be seen that as in Fig. 11, the predicted overall steady-state fracture resistance is between the limits defined by Eqs. 10 and 12. For $J^2_{n,ss}/J^1_{n,ss} \lessapprox 1.5$, the overall steady-state fracture resistance increases linearly with increasing $J^2_{n,ss}$. For $J^2_{n,ss}/J^1_{n,ss} > 1.5$, the overall steady-state fracture resistance first decreases rapidly, then more slowly approaching a value that is 40%-60% higher than if the secondary crack was absent.

It is interesting to note, from Fig. 12, that it is possible to obtain crack propagation of the secondary crack also for $J^2_{n,ss}/J^1_{n,ss} > 1$, *i.e.* when the steady-state fracture resistance of the secondary crack is higher than that of the primary crack.

Fig. 13 shows the overall fracture resistance curve for $J^2_{n,ss}/J^1_{n,ss} = 1.4$ ($\hat{\sigma}^2_n/\hat{\sigma}^1_n = 0.9$). At this $J^2_{n,ss}/J^1_{n,ss}$ ratio, the overall steady-state fracture resistance reaches its maximum value (see Fig. 12), $J_{R,ss}/J^1_{n,ss} \approx 2.2$.

5. Discussion

5.1. Fracture resistance and the openings of the secondary crack

The crack growth mechanism depicted in Fig. 10 shows that the left hand side of the secondary crack does not fully develop but unloads/closes as the secondary crack grows. To further examine the cracking mechanism, the normal crack opening profiles are plotted at different history loading points (see Fig. 9) in Fig. 14 (primary crack) and Fig. 15 (secondary crack) for $h/H = 0.01$, $\hat{\sigma}^2_n/\hat{\sigma}^1_n = 0.5$ and $J^2_{n,ss} = J^1_{n,ss}$ (same parameters as for the results shown by the red curve in Fig. 9). It can be seen that the primary crack opens monotonically with increasing the applied rotational displacements (Fig. 14). On the other hand, as the secondary crack grows (right hand crack tip), its left hand crack tip initially opens but later unloads/closes (Fig. 15). As a result, the overall steady-state fracture resistance, $J_{R,ss}$, approaches the value predicted from Eq. 12. The overall steady-state fracture resistance is approximately 5% lower than Eq. 12 prediction's. This slight difference can be explained by the fact that part of the left hand side of the secondary crack is still open and not completely closed (Fig. 15). The right hand sides of both the primary and the secondary cracks are fully developed; as can be seen from Figs. 14 and 15 the crack openings are larger than the openings at complete failure $\delta^{c,1}_n$ (primary crack) and $\delta^{c,2}_n$ (secondary crack).

Furthermore, the secondary crack growth rate is higher than of the primary crack. At point 10, the crack front of the primary crack is at $x_1/L < 0.3$ (see Fig. 14), whereas the crack tip of the secondary crack is at $x_1/L > 0.5$ (see Fig. 15). This is in agreement with the experimental observations of [24].

As mentioned in Section 3, due to the presence of the secondary crack, the moments in the beam ends of the specimen are not equal. As a consequence, some tangential crack opening is anticipated, mainly for the secondary crack,

and it is plotted in Fig. 16. The tangential crack opening profile for the secondary crack, at different history loading points, displays the same behaviour with the normal opening *i.e.* as the right hand crack tip advances to the right, the left hand side crack tip unloads and closes. However, the magnitude of the opening is much smaller than the tangential opening at complete failure, $\delta_t^{c,2}$. Thus, it can be concluded, that the results presented in the present work correspond to almost pure normal opening.

5.2. Effect of distance h between primary and secondary crack

From Figs. 11 and 12 we note that the overall steady-state fracture resistance approaches its maximum theoretical value (Eq. 12) for small values of h. With increasing h/H the overall steady-state fracture resistance, $J_{R,ss}$, decreases more from its maximum value. The underlying reason for the effect of changing h/H will be discussed next.

Figs. 17 and 18 show the crack opening profile at different history loading points for the primary and secondary crack, respectively, shown in Fig. 9 corresponding to $h/H = 0.1$. The normal crack opening profiles of the primary crack are similar to the normal crack opening profiles for the case of $h/H = 0.01$ (see Fig. 14). The normal crack opening profiles of the secondary crack are also similar to the case of $h/H = 0.01$ but the magnitude of the opening is significantly smaller. As can be seen the normal openings are smaller than the normal opening at complete failure, $\delta_n^{c,2}$ and thus the secondary crack is not fully developed. As a result, the overall steady-state fracture resistance cannot reach the value predicted from Eq. 12. The difference in behaviour for $h/H = 0.01$ and $h/H = 0.1$ can be attributed to the difference in the bending stiffness (the moment of inertia) of the ligament between the two cracking planes (cohesive zones). For $h/H = 0.01$ (Figs. 14 and 15), the bending stiffness is low so that the ligament acts like a slender beam and can easily deform elastically due to the cohesive tractions acting along the ligaments length. As a result, the secondary crack can undergo significant normal opening. In contrast, for $h/H = 0.1$ (Figs. 17 and 18), the bending stiffness of the ligament is so high that the cohesive tractions cannot induce much bending in the ligament. Then, the normal opening of the secondary crack is limited.

5.3. Closure of the left hand crack tip of secondary crack

Fig. 18 also shows that the left hand end of secondary crack initially opens behind the primary crack tip, at negative values of x_1.

Figs. 19 and 20 show the primary and secondary normal crack opening profiles for the history loading points shown in Fig. 13. As mentioned above, this case corresponds approximately to the steady-state fracture resistance of the secondary crack for which the overall steady-state fracture resistance, $J_{R,ss}$, reaches its maximum value following Eq. 12. The normal crack opening profiles for both the primary and secondary crack are similar to the crack opening profiles shown in Figs. 14 and 15 except that the left hand crack tip of the secondary crack (Fig. 20) is now clearly closed. This observation corroborates the theoretical model: Eq. 12 is only realised when the left hand crack tip of the secondary crack is closed.

5.4. Smoothness of fracture resistance curves

The overall fracture resistance curve, see Fig. 13, is smooth up to point 3, which corresponds approximately to the time history where the secondary crack is fully open ($\delta_n^2 = \delta_n^{c,2}$ (see Fig. 20)). Beyond this point, the overall fracture resistance, J_R, curve is non-smooth and this is associated with the discontinuous propagation of two fully developed cracks. The same can be seen in Fig. 9 for $h/H = 0.01$ where the overall fracture resistance curve becomes non-smooth between points 3 and 4. Fig. 15 shows that the secondary crack becomes fully developed between these points. On the other hand, the overall fracture resistance in Fig. 9 for $h/H = 0.1$ is smooth since the normal crack opening of the secondary crack does not reach its critical value $\delta_n^{c,2}$ as can be seen in Fig. 18.

5.5. Factors limiting the maximum attainable fracture resistance

As mentioned, it is possible to obtain propagation of the right hand crack tip of the secondary crack also when $J_{n,ss}^2 > J_{n,ss}^1$, providing that h is sufficiently small. However, as shown in Fig. 12, for $J_{n,ss}^2/J_{n,ss}^1 > 1.5$, the resulting overall steady-state fracture resistance, $J_{R,ss}$, decreases with increasing $J_{n,ss}^2$. This decrease can be understood as follows: With $\hat{\sigma}_n^2$ fixed, an increase in $J_{n,ss}^2$ is (in the finite element model) obtained by increasing $\delta_n^{c,2}$. Then, for high values of $J_{n,ss}^2$, the critical separation, $\delta_n^{c,2}$, may be higher than the opening of the secondary crack, so that the cohesive zone may never be fully developed ($\delta_n^{*,2} < \delta_n^{c,2}$, see Fig. 8) and the work of the normal traction of the right hand crack tip never reaches $J_{n,ss}^2$.

The results presented in Section 4 show that it is possible for a wide range of cohesive law parameters of the secondary crack to obtain close to 85% of the maximum increase in overall steady-state fracture resistance,

given by Eq. 12, if the weak layer (secondary crack) is sufficiently close to the primary crack. The value of the peak stress of the secondary crack is of less importance providing $\hat{\sigma}_n^2 < \hat{\sigma}_n^1$. The proposed approach of increasing the overall fracture resistance by the formation of a secondary crack is thus quite robust.

5.6. Multiple weak layers

The analysis of Section 2 is general for N weak layers. The, the numerical model could be extended to include more weak layers/secondary cracks. In case each new interface crack gives a toughnening increase corresponding to a linear increase of the overall steady-state fracture resistance, $J_{R,ss}$. Therefore, this toughnening approach holds great potential. The approach of using weak layers to increase the overall fracture resistance could be useful in particular to increase the fracture resistance of adhesive joints. Using the results of the present work to carefully design the weak layers, with primary focus on thin layers, damage tolerant adhesive joints could be manufactured.

5.7. Mixed mode cracking

In layered structures, *e.g.* adhesive joints, crack growth often takes place under mixed mode [25]. It will be interesting to extend the current work to mixed mode loading and investigate if the linear dependency between the number of crack tips/fracture process zones and the overall steady state fracture resistance values, Eq. 12, still holds.

5.8. Use of J integral for cohesive laws undergoing closure

Finally, a remark concerning the use of the J integral for the analysis of a cohesive zone that has undergone closure and thus unloading, as shown in Figs. 15, 18 and 20. In analysis of crack growth involving plasticity, the use of J integral is only valid for situations where there is no unloading, so that the non-linear stress-strain relationship of a plastically deforming material is indistinguishable from a non-linear elastic stress-strain law. In the present study, we consider unloading of the left hand side of the secondary crack tip, so that the cohesive law, upon unloading, behaves differently from the opening, which is analogous to unloading during crack growth in an elastic-plastic material. It is therefore relevant to consider if the use of the J integral is still valid under these conditions. It is worth recalling, however, that we analyse cohesive tractions in precisely the same way as any applied tractions. That is, at a given time in the loading history, the analysis uses

the external tractions and cohesive tractions that are present in the specimen at that instance, irrespective of the evolution history. Consequently, the way the cohesive traction has evolved is unimportant. The derived J integral approach is still valid as long as there is no non-elastic unloading in the bulk material.

6. Concluding Remarks

A theoretical model, based on the J integral, predicts that a linear dependency exists between the number of cracks/fracture process zones and the overall steady state fracture resistance. Cohesive zone modelling, consisting of a primary and a secondary crack, was used to identify the cohesive law parameters of the secondary crack for which the linear dependency is approximately valid. It was found that the overall steady state fracture resistance was almost double for a wide range of cohesive law parameters as long as the secondary crack lies close to the primary crack. Thus, it is feasible to increase the fracture resistance of a layered structure significantly by simply adding weak layers. The results of the present work could be used as a guide to select the fracture properties of the weak layers.

Acknowledgement

BFS was supported by the Danish Centre for Composite Structures and Materials for Wind Turbines (DCCSM), Grant No. 09-067212 from the Danish Council for Strategic Research.

References

[1] Kim RY, Soni SR. Experimental and analytical studies on the onset of delamination in laminated composites. Journal of Composite Materials 1984;18:70–80.

[2] Dransfield KA, Jain LK, Mai YW. On the effects of stitching in CFRPs - I. Mode I delamination toughness. Composites Science and Technology 1998;58:815–27.

[3] Mouritz AP. Review of z-pinned composite laminates. Composites Part A 2007;38:2383–97.

[4] Kim JK, Ballie C, Poh J, Mai YW. Fracture toughness of CFRP with modified epoxy matrices. Composites Science and Technology 1992;43:283–97.

[5] Yan C, Xiao K, Ye L, Mai YW. Numerical and experimental studies on the fracture behaviour of rubber-toughened epoxy in bulk specimen and laminated composites. Journal of Materials Science 2002;37:921–7.

[6] Kinloch A, Masania K, Taylor A, Sprenger S, Egan D. The fracture of glassfibre reinforced epoxy composites using nanoparticle-modified matrices. Journal of Materials Science 2008;43:1151–4.

[7] Gojny FH, Wichmann MHG, Kopke U, B BF, Schulte K. Carbon nanotube reinforced epoxy-composites: enhanced stiffness and fracture toughness at low nanotube content. Composites Science and Technology 2004;64:2363–71.

[8] Yeung P, Broutman LJ. The effect of glass-resin interface strength on the impact strength of fibre reinforced plastics. Polymer Engineering & Science 1978;18:62–72.

[9] Madhukar M, Drzal LT. Fibre-matrix adhesion and its relationship to composite mechanical properties. Journal of Materials Science 1993;28:569–610.

[10] Kessler A, Bledzki AK. Correlation between interphase-relevant tests and the impact-damage resistance of glass/epoxy laminates with different surface treatments. Composites Science and Technology 2000;60:125–30.

[11] Feih S, Wei J, Kingshott P, Sørensen BF. The influence of fibre sizing on the strength and fracture toughness of glass fibre composites. Composites Part A 2005;36:245–55.

[12] Ishai O, Rosenthal H, Sela N, Drukker E. Effect of selective adhesive interleaving on interlaminar fracture toughness of graphite/epoxy composite laminates. Composites 1988;19:49–54.

[13] Lu WH, Liao FS, Su AC, Kao PW, Hsu TJ. Effect of interleaving on the impact response of a unidirectional carbon/epoxy composite. Composites 1995;26:215–22.

[14] Sohn MS, Xu XZ. Processing of carbon - fibre/epoxy composites with cost effective interlaminar reinforcement. Composites Science and Technology 1998;58:211–20.

[15] Hojo M, Matsuda S, Tanaka M, Ochiai S, Murakami A. Mode I delamination fatigue properties of interlayer-toughened CF/epoxy laminates. Composites Science and Technology 2006;66:665–75.

[16] Wong DWY, Lin L, McGrail PT, Peijs T, Hogg PJ. Improved fracture toughness of carbon fibre/epoxy composite laminates using dissolvable thermoplastic fibres. Composites Part A 2010;41:759–67.

[17] Hess H, Himmel N. Structurally stitched NCF CFRP laminates. part 1: Experimental characterization of in-plane and out-of-plane properties. Composites Science and Technology 2011;71:549–68.

[18] Falconnet D, Bourban PE, Pandita S, Manson JAE, Verpoest I. Fracture toughness of weft-knitted fabric composites. Composites Part B 2002;33:579–88.

[19] Kim KY, Curiskis JI, Ye L, Fu SY. Mode-I interlaminar fracture behaviour of weft-knitted fabric reinforced composites. Composites Part A 2005;36:957–64.

[20] Mouritz AP, Bannister MK, Falzon PJ, Leong KH. Review of applications of advanced three-dimensional fibre textile composites. Composites Part A 1999;30:1445–61.

[21] Mouritz AP, Baini C, Herszberg I. Mode I interlaminar fracture toughness properties of advanced textile fibreglass composites. Composites Part A 1999;30:859–70.

[22] Rugg KL, Cox BN, Massabo R. Mixed mode delamination of polymer composite laminates reinforced through the thickness by z-fibers. Composites Part A 2002;33:177–90.

[23] Chang P, Mouritz AP, Cox BN. Properties and failure mechanisms of z-pinned laminates in monotonic and cyclic tension. Composites Part A 2006;37:1501–13.

[24] Rask M, Sørensen BF. Determination of the J integral for laminated double cantilever beam specimens: The curvature approach. Engineering Fracture Mechanics 2012;96:37–48.

[25] Sørensen BF, Goutianos S, Jacobsen TK. Strength scaling of adhesive joints in polymer-matrix composites. International Journal of Solids and Structures 2009;46:741–61.

[26] Rice JR. A path independent integral and the approximate analysis of strain concentrations by notches and cracks. Journal of Applied Mechanics 1968;35:379–86.

[27] Sills RB, Thouless MD. Cohesive-length scales for damage and toughening mechanisms. International Journal of Solids and Structures 2014;in press.

[28] Gong SX, Horii H. General-solution to the problem of microcracks near the tip of a main crack. Journal of the Mechanics and Physics of Solids 1989;37:27–46.

[29] Shum DKM, Hutchinson JW. On toughening by microcracks. Mechanics of Materials 1990;9:83–91.

[30] Dugdale DS. Yielding of steel sheets containing slits. Journal of the Mechanics and Physics of Solids 1960;8:100–4.

[31] Barenblatt G. The mathematical theory of equilibrium cracks in brittle fracture. Advances in Applied Mechanics 1962;7:55–129.

[32] Hillerborg A. Application of the fictitious crack model to different types of materials. International Journal of Fracture 1991;51:95–102.

[33] Abaqus Version 6.11 . Abaqus Inc; 2012.

[34] Sørensen BF, Goutianos S. Mixed mode cohesive law with interface dilatation. Mechanics of Materials 2014;70:76–93.

[35] Belytschko T, Liu WK, Moran B. Nonlinear Finite Elements for Continua and Structures. New York: Wiley; 2000.

[36] Bao G, Ho S, Suo Z, Fan B. The role of material orthotropy in fracture specimens for composites. International Journal of Solids and Structures 1992;29:1105–16.

[37] Sørensen BF, Jørgensen K, Jacobsen TK, Østergaard RC. DCB-specimen loaded with uneven bending moments. International Journal of Fracture 2006;141:163–76.

[38] Yang QD, Thouless MD. Mixed-mode fracture analyses of plastically-deforming adhesive joints. International Journal of Fracture 2001;110:175–87.

[39] Li S, Thouless MD, Waas AM, Schroeder JA, Zavattieri PD. Mixed-mode cohesive-zone models for fracture of an adhesively bonded polymermatrix composite. Engineering Fracture Mechanics 2006;73:64–78.

[40] Wang JS, Suo Z. Experimental determination of interfacial toughness curves using Brasil-nut-sandwiches. Acta Metallurgica et Materialia 1990;38:1279–90.

[41] Goutianos S, Sørensen BF. Path dependence of truss-like mixed mode cohesive laws. Engineering Fracture Mechanics 2012;91:117–32.

Figure

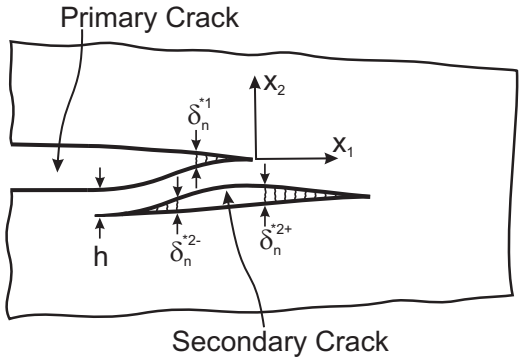

Figure 1: Cracking in a weak layer (secondary crack) located at distance h from the primary crack. $\delta_n^{*,1}$ is the normal end-opening of the primary crack and $\delta_n^{*,2-}$ and $\delta_n^{*,2+}$ the normal end-openings of the right and left hand side crack tips of the secondary crack.

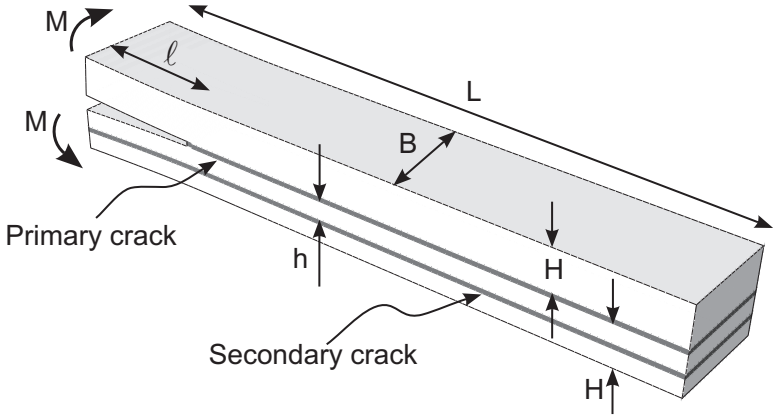

Figure 2: Double Cantilever Beam (DCB) specimen subjected to pure bending moments, M. A notch of length ℓ is used to initiate the primary crack. A second, potential, crack is defined at a distance h from the primary crack.

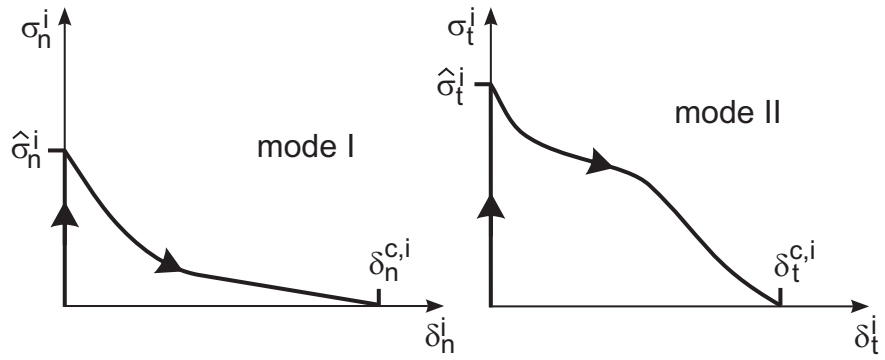

Figure 3: Schematic of cohesive laws.

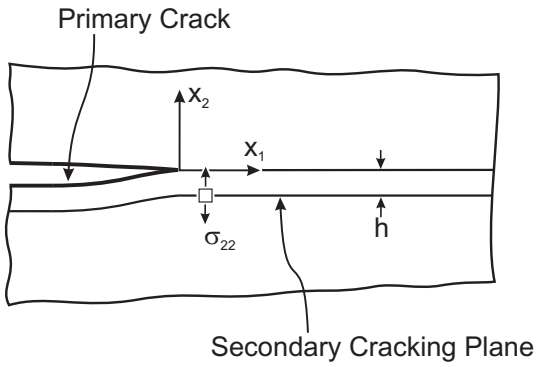

(a)

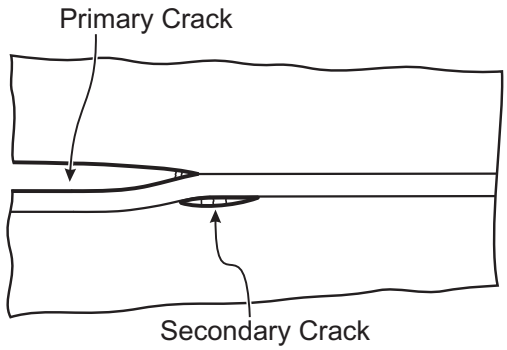

(b)

Figure 4: Local J integral path enclosing the primary and secondary crack.

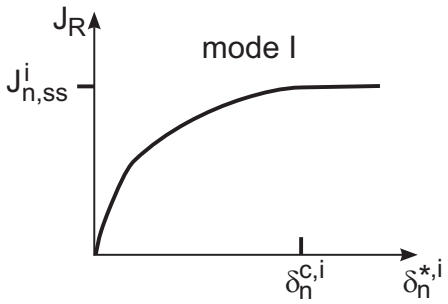

Figure 5: Schematic of fracture resistance curve.

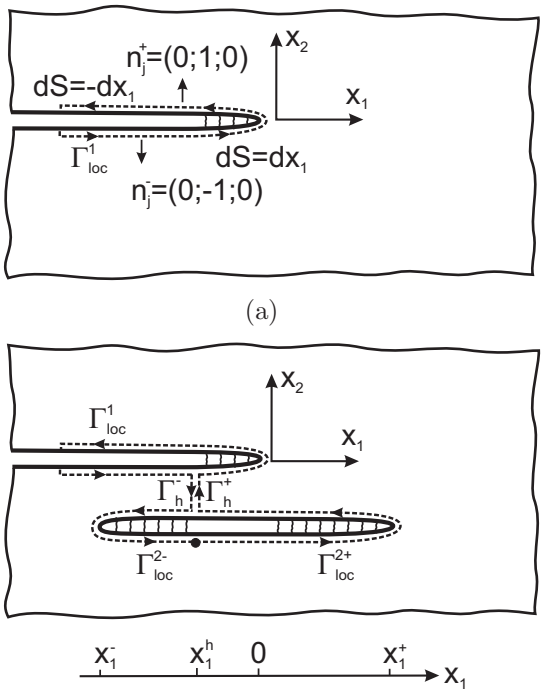

Figure 6: Local J integral path enclosing the primary and secondary crack.

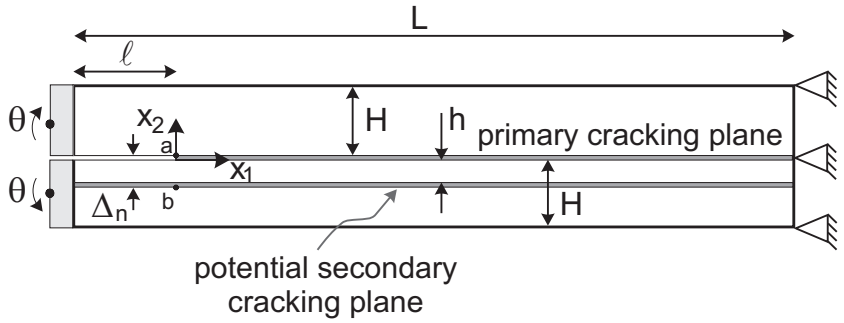

Figure 7: Geometry, loads and boundary conditions of the finite element model. The potential cracking planes, which are modeled by cohesive zones, are indicated.

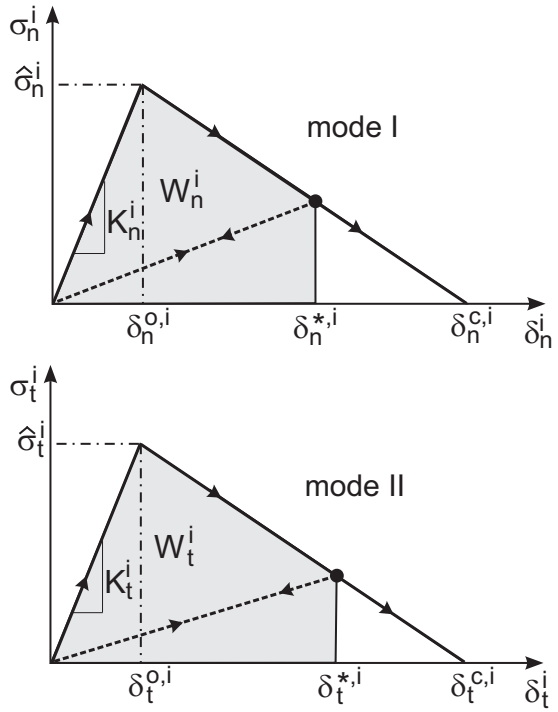

Figure 8: Mode I and mode II linear softening cohesive laws, respectively, for the primary ($i = 1$) and secondary crack ($i = 2$).

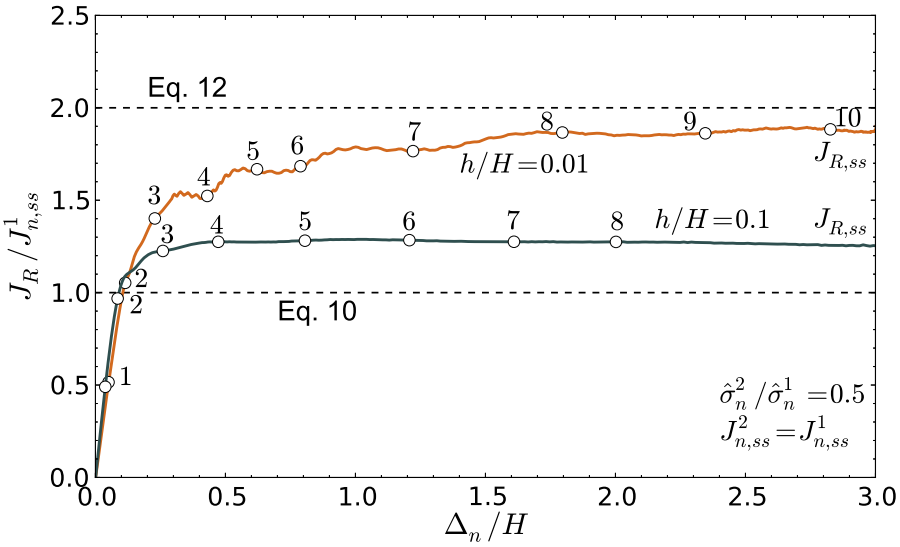

Figure 9: Overall fracture resistance, J_R, as a function of the end-opening, Δ_n, comprising the end-openings of the primary crack, δ_n^1, the secondary crack, δ_n^2, and the deformation of the ligament between the two cracks (see Fig. 7: distance between points a and b).

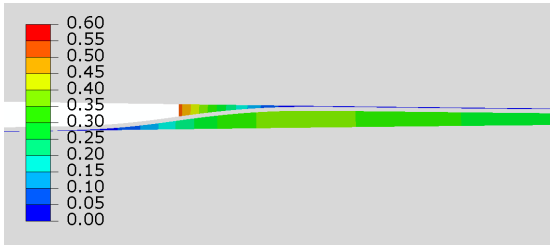

(a) Point 1

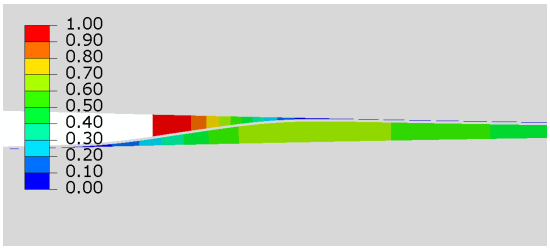

(b) Point 2

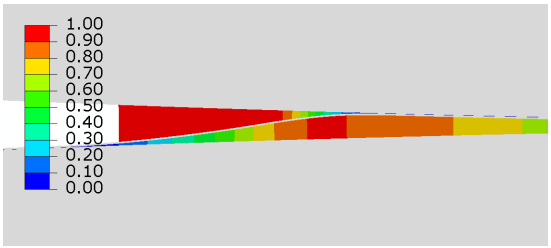

(c) Point 3

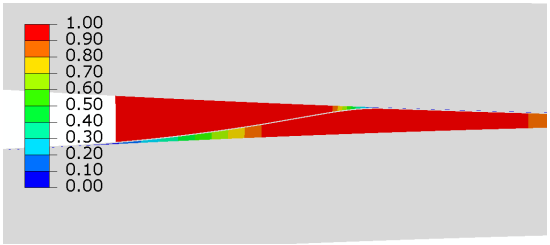

(d) Point 4

Figure 10: Contour plots of the failure criterion (Eq. 15) for $\hat{\sigma}_n^2/\hat{\sigma}_n^1 = 0.5$ and $h/H = 0.01$. The points correspond to the loading history points of Fig. 9. The colour code indicates the magnitude of the openings within the cohesive zone, blue (contour level 0.00) indicates a completely closed state; red (contour level 1.00) fully open.

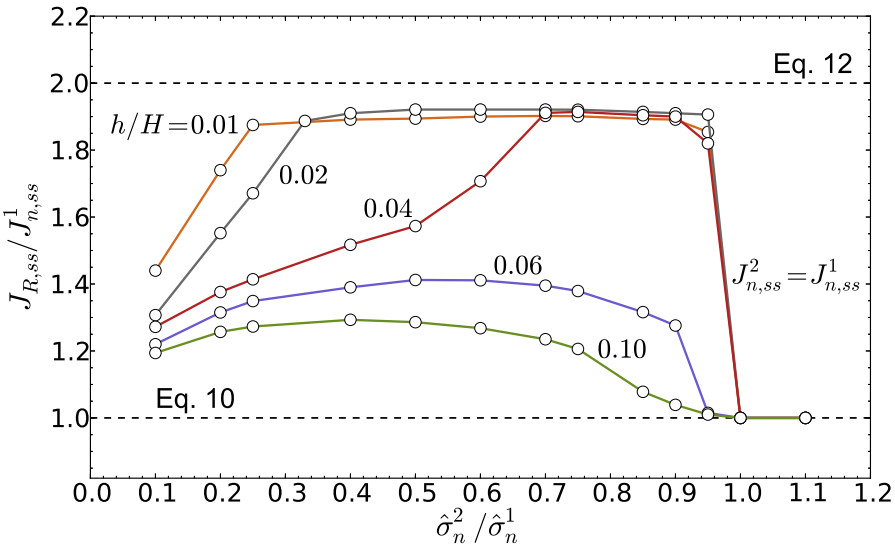

Figure 11: Overall steady-state fracture resistance, $J_{R,ss}$, as a function of the peak traction of the secondary crack, $\hat{\sigma}^2_n$ for both the primary and secondary crack. The cohesive law of the shear traction is identical to the cohesive law of the normal traction, respectively.

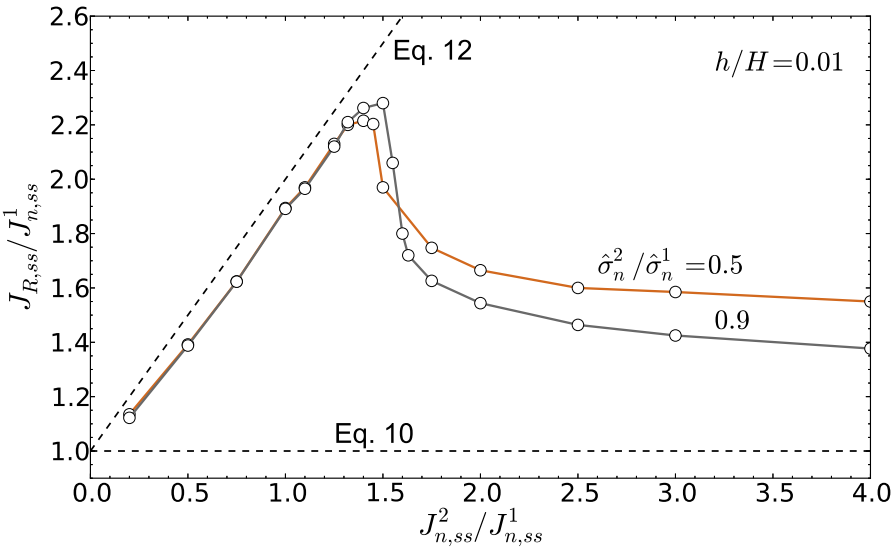

Figure 12: Overall steady-state fracture resistance, $J_{R,ss}$, enhancement as a function of the steady-state fracture resistance of the secondary crack, $J_{n,ss}^2$. The Mode II cohesive law is identical to the Mode I cohesive law for the primary and secondary crack, respectively.

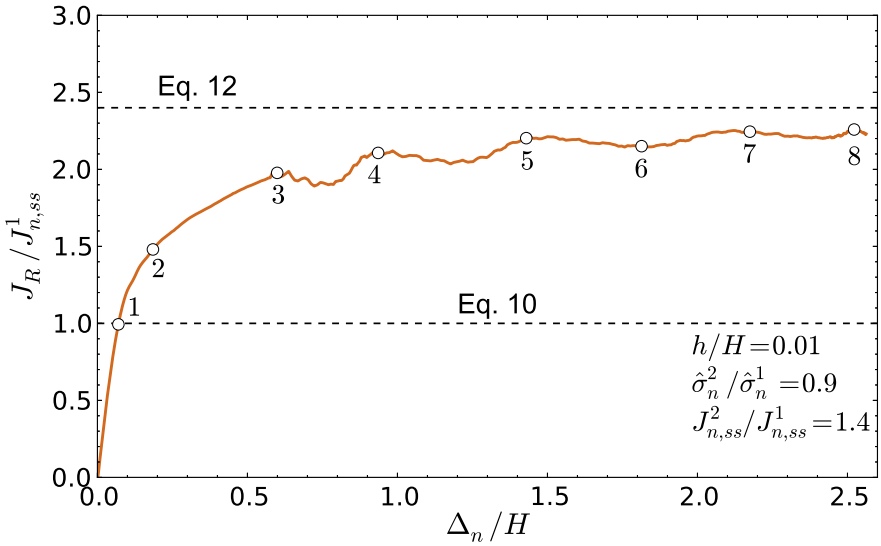

Figure 13: Overall fracture resistance, J_R, as a function of the end-opening, Δ_n, comprising the end-openings of the primary crack, δ_n^1, the secondary crack, δ_n^2, and the deformation of the material between the two cracks (see Fig. 7: distance between points a and b).

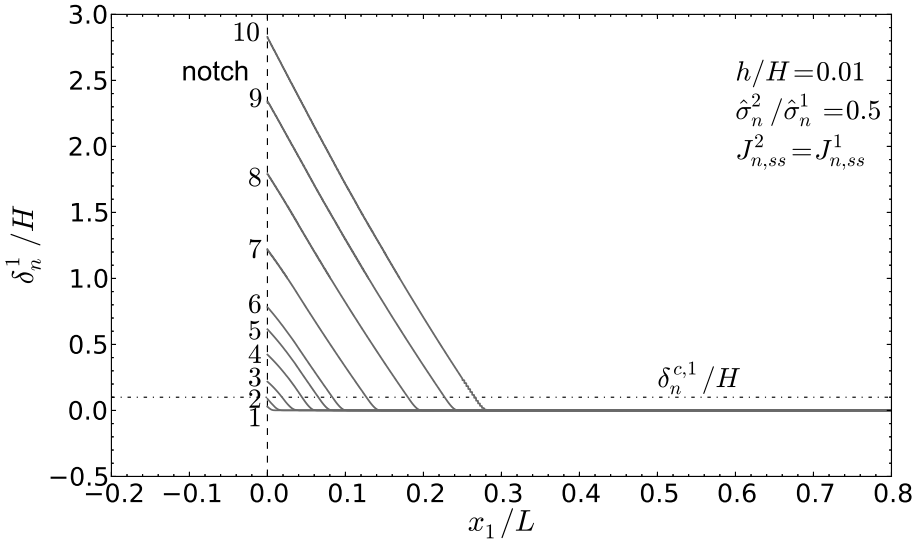

Figure 14: Normal crack opening profiles of the primary crack for the history loading points (1-10) shown in Fig. 9 ($h/H = 0.01$).

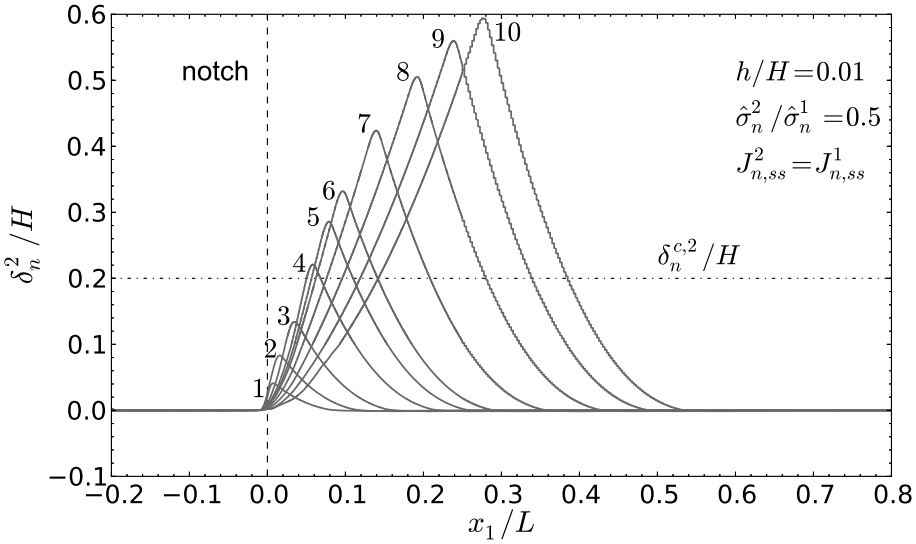

Figure 15: Normal crack opening profile of the secondary crack for the history loading points (1-10) shown in Fig. 9 ($h/H = 0.01$).

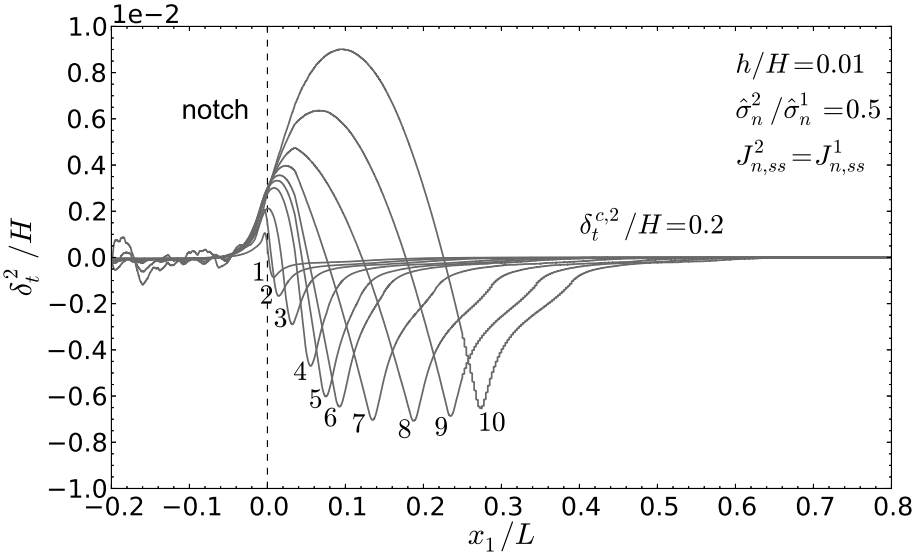

Figure 16: Tangential crack opening profile of the secondary crack for the history loading points (1-10) shown in Fig. 9 ($h/H = 0.01$).

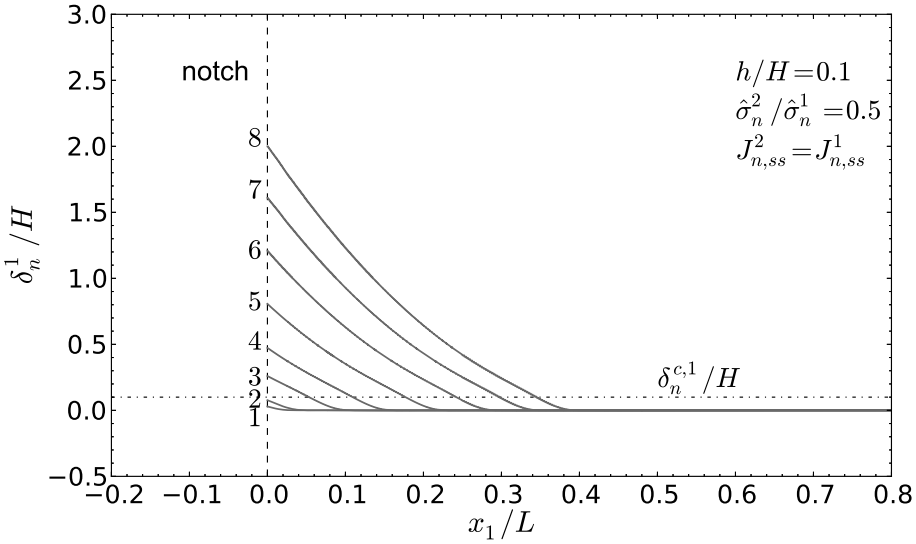

Figure 17: Normal crack opening profile of the primary crack for the history loading points (1-8) shown in Fig. 9 ($h/H = 0.1$).

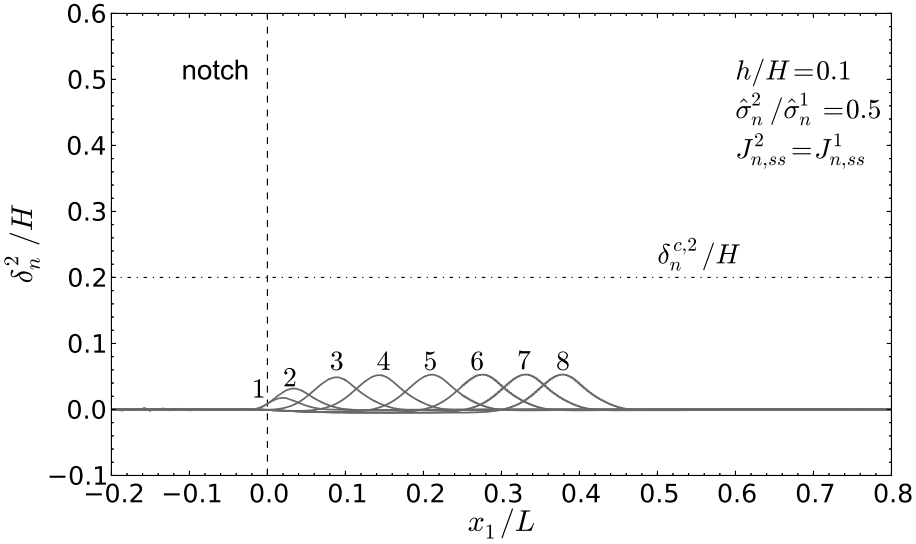

Figure 18: Normal crack opening profile of the secondary crack for the history loading points (1-8) shown in Fig. 9 ($h/H = 0.1$).

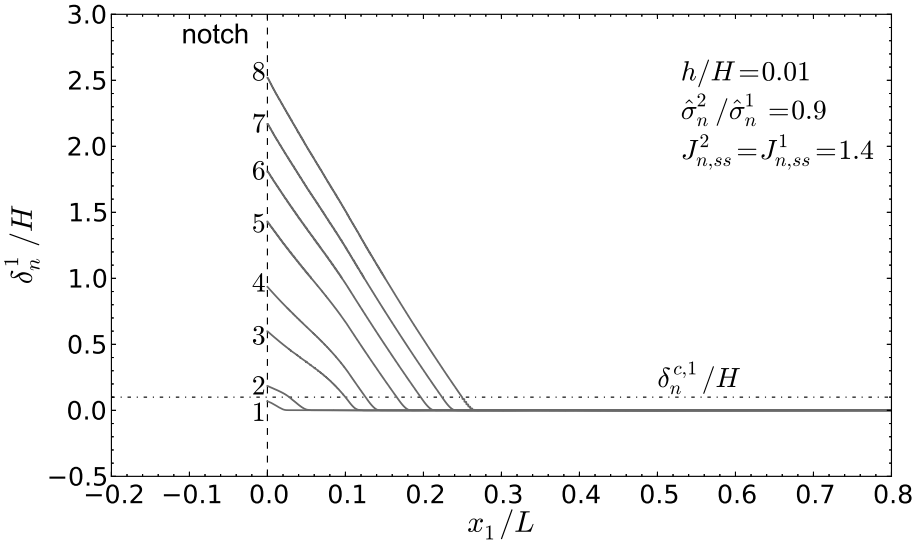

Figure 19: Normal crack opening profile of the primary crack for the history loading points (1-8) shown in Fig. 13.

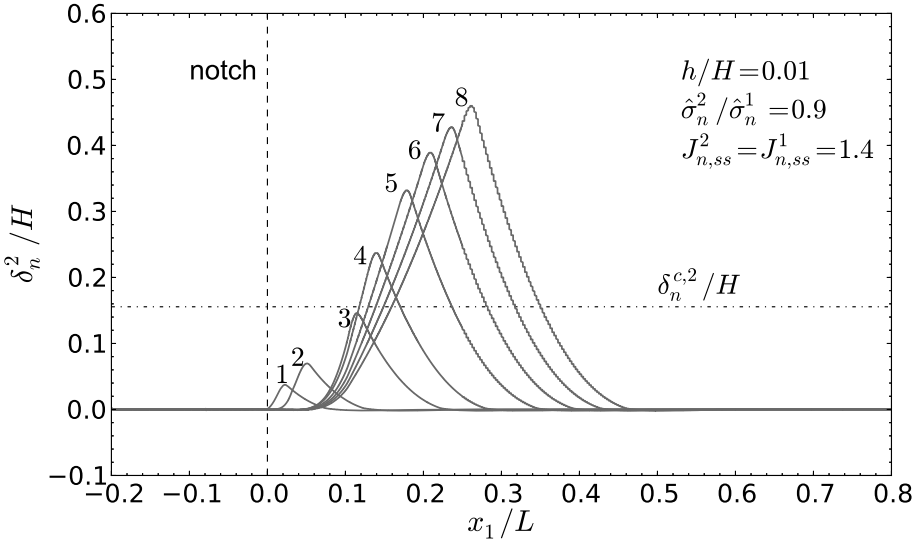

Figure 20: Normal crack opening profile of the secondary crack for the history loading points (1-8) shown in Fig. 13.